Thermo-poro-viscoelastic response of a disc-shaped inclusion

Massimo Nespoli [ID], Maria Elina Belardinelli [ID] and Maurizio Bonafede

Department of Physics and Astronomy, "Augusto Righi", Alma Mater Studiorum, Università di Bologna, Viale Berti Pichat 6/2, 40127, Bologna, Italy .
E-mail: massimo.nespoli2@unibo.it

SUMMARY
The study of deformation sources in volcanic and geothermal fields is a topic of great importance that generates a large debate in the scientific literature. A correct interpretation of the deformation sources acting in a volcanic context is crucial to distinguish between the mechanical effects due to the tectonic of the area, the intrusion of new magma and/or the mechanical response of rocks to temperature or pore pressure changes. In the recent literature, thermo-poro-elastic (TPE) inclusions were proposed as possible deformation sources that can explain seismicity and displacements even in absence of the emplacement of new magma. In fact, TPE inclusions allow us to compute the mechanical effects due to temperature and pore-pressure changes brought by the arrival of hot and pressurized fluids permeating a closed volume. In the present work, we improve the modellization of such deformation sources to include the effects of viscoelasticity, which should be expected in high temperature and fluid saturated rocks due to thermally activated and pressure-solution creep. The analytical thermo-poro-viscoelastic (TPVE) solutions for a disc-shaped inclusion embedded in a uniform viscoelastic medium are obtained through the correspondence principle. Our results can be useful to represent transient effects of both deformation and stress fields that can occur in both volcanic and geothermal areas, which would be difficult to explain otherwise. In fact, TPE inclusion models predict that an increase of uplift occurs simultaneously with an increase of stress, and vice versa. Instead, we shall see that a TPVE inclusion can provide an increase of uplift even in presence of a strongly decreasing deviatoric stress. For this reason, a TPVE inclusion can be suitable to represent a decrease in seismicity rate accompanied by an increase in surface uplift, as observed, for example, during the '82–'84 unrest phase of Campi Flegrei in Italy.

Key words: Elasticity and anelasticity; Hydrothermal systems; Transient deformation; Induced seismicity; Calderas.

1 INTRODUCTION

The inclusion method (Eshelby 1957) can be used to model the mechanical effects of a volume (i.e. an inclusion) that undergoes temperature and pore-pressure changes, enclosed by an elastic medium. Such a method is well known in the literature as it is suitable to model the deformation induced by geothermal reservoirs and to study their potential to induce seismicity (Geertsma 1973; Segall 1992; Rudnicki 1999; Guido *et al.* 2015). In particular, since the pioneering works of Segall (1989) and Segall & Fitzgerald (1998), it has been well known that thermo-poro-elastic (TPE) inclusions can be useful to explain the different fault mechanisms induced by oil and gas production inside and around the reservoirs.

More recently, the inclusion method was applied to study the mechanical effects of TPE inclusions in volcanic environments, where pore-pressure and temperature changes derive from the exsolution of fluids of magmatic origin (e.g. Belardinelli *et al.* 2019; Mantiloni *et al.* 2020; Nespoli *et al.* 2021). To date, the most intriguing results of the application of TPE inclusions in geothermal and volcanological contexts can be summarized as follows: (*i*) they easily allow to estimate deformation and stress fields due to the injection or withdrawal of hydrothermal fluids; (*ii*) differently from pressurized cavities (e.g. fluid filled magma chambers), they create a strong deviatoric stress field even within the source region; (*iii*) they may explain significant deformations even in environments in which there are no evidences of shallow large magmatic bodies; and (*iv*) they can explain the heterogeneity of fault mechanisms of induced earthquakes located at close distance.

Belardinelli *et al.* (2019) proposed analytical solutions to model TPE inclusions with spherical and spherical shell geometries, embedded in a full space. The latter geometry can be used, for example, to represent a TPE shell volume that separates a spherical magma chamber from the external embedding elastic medium. The fully analytical solutions for disc-shaped TPE inclusions embedded in an elastic space were then
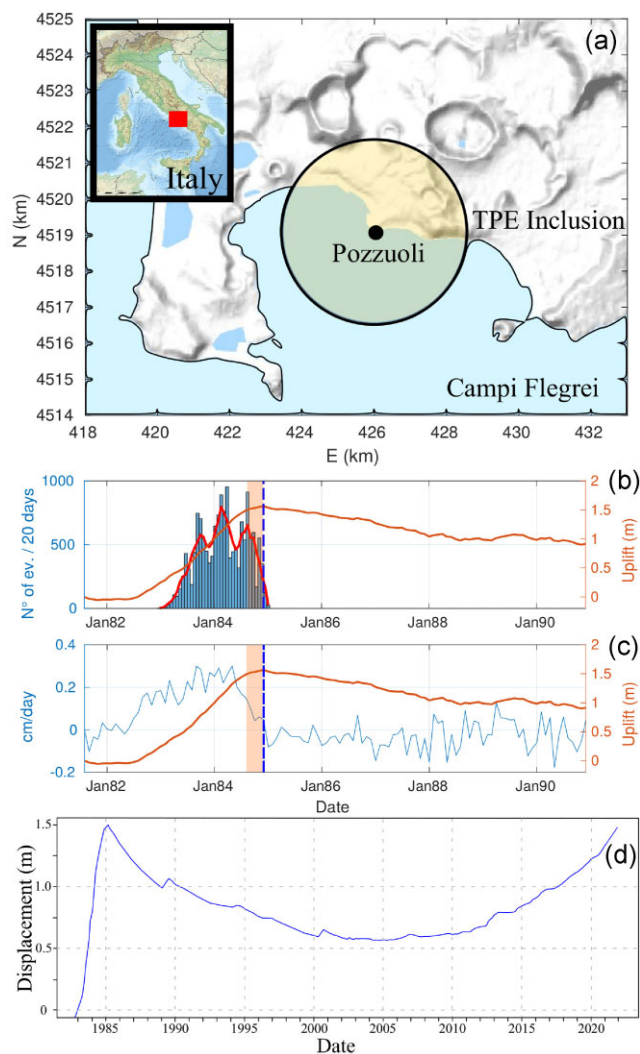
Figure 1. (a) Caldera of Campi Flegrei (Italy). The yellow circle represents the projection of the TPE inclusion as inferred from the inversion of geodetic data measured during the period June 1980–1983 (Nespoli et al.2021). (b) Vertical displacement (orange curve) as a function of time, measured in the location of maximum measured uplift (Pozzuoli harbour) from 1980 to 1990. Histograms represent the number of events in time windows of 20 d. The red curve shows the number of events computed with a moving average. (c) Vertical displacement (orange curve) as a function of time plotted together with the uplift rate (light blue curve, cm d^{-1}). The blue dashed line represents the end of the uplift phase. The orange area indicates the time interval before the end of the uplift phase that was characterized by a decrease of both uplift rate and seismicity rate. Data from Belardinelli *et al.*(2011). (d) Long time-series of vertical displacement measured at Pozzuoli between 1983 and 2022 (De Martino *et al.*2021).

computed by Belardinelli *et al.* (2022). Such a geometry is better suited to describe horizontally extended permeable rock layers stressed and strained by hot and pressurized volatiles released into a flat, nearly circular region, as usually occurs inside a volcano caldera. Mantiloni *et al.* (2020) presented semi-analytical solutions to model a disc-shaped TPE inclusion embedded in an elastic half-space. The solutions computed in a half-space offer, in particular, the possibility of modelling the displacement at the surface. Therefore, they can be useful to compare model results with more geophysical observables and they allow us to perform geodetic data inversions to infer deformation source parameters. More recently, Nespoli *et al.* (2021) showed how the solutions of Mantiloni *et al.* (2020) can be extended to thick, cylindrical TPE inclusions, embedded in a layered elastic half-space. Their solutions rely on the fact that the mechanical effects of TPE inclusions can be physically described through a distribution of single forces acting normally on the surface of the inclusion, as generally, inelastic deformations can be represented by an appropriate distribution of equivalent body forces (e.g. Landry & Barbot 2019). Based on the distribution of equivalent forces, the mechanical effects of a TPE inclusion with an arbitrary shape, located in a layered elastic half-space, can be modelled with the propagator method using the *EFGRN/EFCMP* code (Nespoli *et al.* 2022).

Several recent applications of TPE inclusion models in a volcanological context are focused on the caldera of Campi Flegrei (Italy). There, the volcanic activity started about 39 000 years ago (De Vivo *et al.* 2001) and was characterized by several episodes of bradyseism (Di Vito *et al.* 1999). During the unrest phase occurred in 1982–1984, a maximum uplift of 1.8 m was measured close to the centre of the caldera (Del Gaudio *et al.* 2010), located near the city of Pozzuoli. This bradiseismic episode (Fig. 1) was characterized by thousands of earthquakes (D'Auria *et al.* 2014). Few months before the end of the uplift phase, seismicity declined (Barberi *et al.* 1984; Belardinelli *et al.*

2011), as shown in Fig. 1. After that period, there were 20 yr of prevailing subsidence. A new uplift phase started in 2005 (Fig. 1d), and it is still continuing today; it was accompanied by an increase of both fumarole activity and seismicity rate (Tramelli *et al.* 2021).

In the literature, the debate about the nature of the sources inducing the deformation of Campi Flegrei is still open. In fact, the soil deformation can be effectively described by both pressurized, magma filled cavities and TPE inclusion models. From high-resolution seismic tomography, Judenherc & Zollo (2004) and Carlino *et al.* (2012) exclude the presence of large magmatic bodies in the shallowest 2 km of depth. Trasatti *et al.* (2011) succeeded in reproducing the observed uplift employing a complex magma filled dislocation source at 4.5 km depth, and similarly, D'Auria *et al.* (2015) interpreted the deformation as due to a sill intrusion at about 3 km of depth. However, a non magmatic deformation source can be also considered. For this reason, a significant part of the literature focuses on the importance of considering the hydrothermal circulation (e.g. Chiodini *et al.* 2021; Nespoli *et al.* 2021; Todesco 2021) as a relevant mechanism to justify, at least partially, the deformation and the seismicity observed at Campi Flegrei. According to these authors, hydrothermal fluids were supplied by a deep magmatic chamber to a shallower volume, located above 3 km of depth, where most of the seismicity occurred during 1982–1984 unrest phase (Tramelli *et al.* 2022). According to Lima *et al.* (2021), Calò & Tramelli (2018), Nespoli *et al.* (2022) and ref. therein, such a volume cyclically allows or prevents the rising of the magmatic fluids from depth, acting as a valve. The location and geometry of such a volume was obtained by geodetic data inversion by Nespoli *et al.* (2021). They found that both the seismicity and the deformation of the '82–'84 unrest can be well reproduced employing a cylindrical TPE inclusion located at a depth of about 2 km, with a radius of about 2.5 km and a thickness of 500 m.

Solid–fluid interaction is a highly complex process. A realistic description of hydrothermal circulation requires to account for the complex properties of both solid and fluid phases and their mutual coupling. Some hints were provided by Belardinelli *et al.* (2022) on the basis of some simplifying assumptions. Even numerical approaches must be based on more or less strong assumptions and simplifications. Following Belardinelli *et al.* (2022), we believe that the analytical approaches allow us to better understand the physical phenomena at the base of the problem. Furthermore, they allow us to create a starting point for more complicated numerical models. One of the possible complications of TPE models consists in considering a viscoelastic behaviour of the medium containing the inclusion (e.g. Kazemi-Lari *et al.* 2021). The viscoelastic rheological properties of the medium can be extremely important to model the deformation, especially in volcanic and geothermal regions (Bonafede & Ferrari 2009), which are characterized by high temperatures, promoting thermally activated creep (e.g. Wang 2021; Goetze & Evans 1979), high fluid pressures, promoting pressure-solution creep (e.g. Gratier *et al.* 2013) and high deviatoric stress, overcoming the plastic threshold. Furthermore, we will see that differently from a TPE inclusion, a thermo-poro-viscoelastic (TPVE) inclusion could explain the time-lag, which can occur between the decreases of uplift and seismicity rate, as was observed at Campi Flegrei (Fig. 1).

A TPVE medium can be envisaged as a rock matrix with viscoelastic behaviour containing fluid-filled and interconnected cavities. The fluid migration allows transmission of heat and pore pressure by means of advection, which is a very efficient process in high permeability media. The implementation of the viscoelastic behaviour can be attained using the correspondence principle (Fung 1965). In this study, we will assume a Maxwell rheology that is the simplest choice. In this case, differently from what was expected according to other linear rheologies [e.g. Standard Linear Solid (SLS)], the complete relaxation of additional deviatoric stress takes place. In the following, we will show how the viscoelastic behaviour may be simply introduced, starting from the analytic solutions of a TPE disc (Mantiloni *et al.* 2020; Belardinelli *et al.* 2022).

2 TPE SOLUTIONS

For a TPE medium, we have the following constitutive equation expressing the strain e_{ij} as function of stress σ_{ij} and changes of pore pressure p and temperature T:

$$e_{ij} = \frac{1}{2\mu} \left(\sigma_{ij} - \frac{\nu}{1+\nu} \sigma_{kk} \delta_{ij} \right) + e_0 \delta_{ij} \tag{1}$$

with

$$e_0 = \frac{1}{3H} p + \frac{1}{3} \alpha_s T \tag{2}$$

where ν is the drained isothermal Poisson's ratio, μ the rigidity, $1/H$ is the poroelastic expansion and α_s the thermal expansion coefficient of the solid matrix. The parameter e_0 is the "inclusion potency" (Nespoli *et al.* 2021, 2022). In the case of a TPE inclusion, the displacement (Eshelby 1957) can be expressed as

$$u_i(\mathbf{x}) = \oint_S 3K e_0 G_{ik}(\mathbf{x}, \mathbf{x}') n_k(\mathbf{x}') dS', \tag{3}$$

where the integral is computed over the surface S surrounding the inclusion (e.g. Aki & Richards 2002; Belardinelli *et al.* 2019). In equation (3), $K = \frac{2\mu(1+\nu)}{3(1-2\nu)}$ is the drained isothermal bulk modulus of the medium, $G_{ik}(\mathbf{x}, \mathbf{x}')$ is the Green's tensor representing the $i - th$ component of displacement at $\mathbf{x}$ due to a single (and unitary) point force, acting in the $k - th$ direction, located in $\mathbf{x}'$. In a homogeneous half-space, $G_{ik}(\mathbf{x}, \mathbf{x}')$ is given by the sum of singular terms (when $\mathbf{x} = \mathbf{x}'$) representing the Green function in a full space, and non-singular terms representing the free surface contributions. Notice that, according to equation (3), the displacement of a TPE inclusion linearly scales with the inclusion
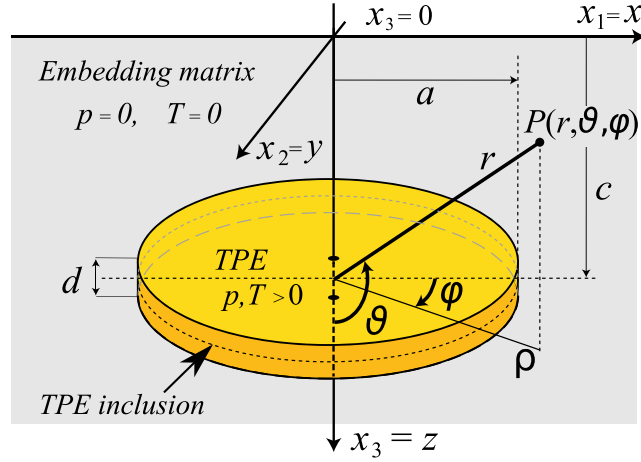
Figure 2. Reference systems used to represent the TPE disc (yellow volume) embedded in elastic matrix (grey).

potency e_0. The strain field e_{ij} can be computed according to the infinitesimal strain theory as

$$e_{ij} = \frac{1}{2}\left(\frac{\partial u_i}{\partial x_j} + \frac{\partial u_j}{\partial x_i}\right) \tag{4}$$

The stress field, can be computed from (3) as

$$\sigma_{ij}(\mathbf{x}) = \begin{cases} \lambda e_{kk}\delta_{ij} + 2\mu e_{ij} - 3Ke_0\delta_{ij}, & \mathbf{x} \in V_S \\ \lambda e_{kk}\delta_{ij} + 2\mu e_{ij}, & \mathbf{x} \notin V_S \end{cases} \tag{5}$$

where V_S is the volume of the inclusion enclosed by the surface S. Notice the additional term $-3Ke_0\delta_{ij}$, appearing inside the inclusion (e.g. Barbot 2018; Belardinelli *et al.* 2019, 2022).

According to Mantiloni *et al.* (2020), for a disc-shaped TPE inclusion with radius a (Fig. 2), embedded in a half-space with free surface in $z = 0$, the solutions can be obtained considering two different contributions: a singular component (superscript s) that can be computed analytically and a non-singular component (superscript ns) that can be computed semi-analytically from the full space solution of Belardinelli *et al.* (2022). So that the displacement and the strain can be computed as:

$$u_i(\mathbf{x}) = u_i^s(\mathbf{x}) + u_i^{ns}(\mathbf{x}) \tag{6a}$$

$$e_{ij}(\mathbf{x}) = e_{ij}^s(\mathbf{x}) + e_{ij}^{ns}(\mathbf{x}) \tag{6b}$$

and the stress

$$\sigma_{ij}(\mathbf{x}) = \begin{cases} \sigma_{ij}^s(\mathbf{x}) + \sigma_{ij}^{ns}(\mathbf{x}) - 3Ke_0\delta_{ij}, & \mathbf{x} \in V_S \\ \sigma_{ij}^s(\mathbf{x}) + \sigma_{ij}^{ns}(\mathbf{x}), & \mathbf{x} \notin V_S \end{cases}. \tag{7}$$

In Section 3, we will apply the correspondence principle to both singular and non-singular components, separately, in order to obtain the quasi-static time-dependent solutions in a homogeneous Maxwell half-space.

2.1 Singular components of displacement and strain

The singular components of displacement and strain were computed in spherical coordinates (Fig. 2) by Belardinelli *et al.* (2022). First, we rewrite them in order to factor out the quantities that depend on the elastic parameters of the medium. Accordingly, the radial and polar components can be written as:

$$u_r^s(\mathbf{r}) = \begin{cases} Aa\,S_1(\mathbf{r}) \text{ if } r < a \\ Aa\,S_2(\mathbf{r}) \text{ if } r > a \end{cases}, \quad u_\theta^s(\mathbf{r}) = \begin{cases} Aa\,S_3(\mathbf{r}) \text{ if } r < a \\ Aa\,S_4(\mathbf{r}) \text{ if } r > a \end{cases} \tag{8}$$

where S_{1-4} do not depend on elastic parameters and are expressed by series expansions (Appendix A) and the coefficient A is

$$A = e_0\frac{d}{2a}\frac{1+\nu}{1-\nu} \tag{9}$$

The non-vanishing components of strain can be written as following in terms of series expansions S_{5-12} (Appendix A):

$$e_{rr}^s = \begin{cases} AS_5(\mathbf{r}) \text{ if } r < a \\ AS_6(\mathbf{r}) \text{ if } r > a \end{cases}, \quad e_{\theta\theta}^s = \begin{cases} AS_7(\mathbf{r}) \text{ if } r < a \\ AS_8(\mathbf{r}) \text{ if } r > a \end{cases}, \tag{10a}$$

$$e^s_{\varphi\varphi} = \begin{cases} AS_9(\mathbf{r}) \text{ if } r < a \\ AS_{10}(\mathbf{r}) \text{ if } r > a \end{cases}, \; e^s_{r\theta} = \begin{cases} AS_{11}(\mathbf{r}) \text{ if } r < a \\ AS_{12}(\mathbf{r}) \text{ if } r > a \end{cases}. \tag{10b}$$

2.2 Non-singular components of displacement and strain

The non-singular components were computed by Mantiloni *et al.* (2020) and can be rewritten as:

$$u^{ns}_1(\mathbf{x}) = 3KBe_0\left[(3-4\nu)I^{(1)}_a(\mathbf{x}) + I^{(1)}_b(\mathbf{x})\right] = CI^{(1)}_a(\mathbf{x}) + DI^{(1)}_b(\mathbf{x}) \tag{11a}$$

$$u^{ns}_2(\mathbf{x}) = 3KBe_0\left[(3-4\nu)I^{(2)}_a(\mathbf{x}) + I^{(2)}_b(\mathbf{x})\right] = CI^{(2)}_a(\mathbf{x}) + DI^{(2)}_b(\mathbf{x}) \tag{11b}$$

$$u^{ns}_3(\mathbf{x}) = -3KBe_0\left[(3-4\nu)I^{(3)}_a(\mathbf{x}) + I^{(3)}_b(\mathbf{x})\right] = -CI^{(3)}_a(\mathbf{x}) - DI^{(3)}_b(\mathbf{x}) \tag{11c}$$

where

$$B = \frac{1-2\nu}{8\pi\mu(1-\nu)} \tag{12a}$$

$$C = 3KBe_0(3-4\nu) \tag{12b}$$

$$D = 3KBe_0 \tag{12c}$$

The explicit expression of $I^{(1-3)}_a$ and $I^{(1-3)}_b$ are reported in Appendix A. The non-singular components of strain can be computed from displacement as:

$$e^{ns}_{11}(\mathbf{x}) = 3KBe_0\left[(3-4\nu)\frac{\partial I^{(1)}_a}{\partial x_1} + \frac{\partial I^{(1)}_b}{\partial x_1}\right] = C\frac{\partial I^{(1)}_a}{\partial x_1} + D\frac{\partial I^{(1)}_b}{\partial x_1} \tag{13a}$$

$$e^{ns}_{22}(\mathbf{x}) = 3KBe_0\left[(3-4\nu)\frac{\partial I^{(2)}_a}{\partial x_2} + \frac{\partial I^{(2)}_b}{\partial x_2}\right] = C\frac{\partial I^{(2)}_a}{\partial x_2} + D\frac{\partial I^{(2)}_b}{\partial x_2} \tag{13b}$$

$$e^{ns}_{33}(\mathbf{x}) = -3KBe_0\left[(3-4\nu)\frac{\partial I^{(3)}_a}{\partial x_3} + \frac{\partial I^{(3)}_b}{\partial x_3}\right] = -C\frac{\partial I^{(3)}_a}{\partial x_3} - D\frac{\partial I^{(3)}_b}{\partial x_3} \tag{13c}$$

$$\begin{aligned} e^{ns}_{13}(\mathbf{x}) &= \frac{3KBe_0}{2}\left[(3-4\nu)\left(\frac{\partial I^{(1)}_a}{\partial x_3} + \frac{\partial I^{(3)}_a}{\partial x_1}\right) + \frac{\partial I^{(1)}_b}{\partial x_3} + \frac{\partial I^{(3)}_b}{\partial x_1}\right] \\ &= \frac{C}{2}\left(\frac{\partial I^{(1)}_a}{\partial x_3} + \frac{\partial I^{(3)}_a}{\partial x_1}\right) + \frac{D}{2}\left(\frac{\partial I^{(1)}_b}{\partial x_3} + \frac{\partial I^{(3)}_b}{\partial x_1}\right) \end{aligned} \tag{13d}$$

The explicit expression of the derivatives are reported in Appendix A.

3 TPVE SOLUTIONS

The deformation provided by Maxwell rheology, for large times, can be considered as an upper bound of the one provided by other rheological models (Bonafede & Ferrari 2009). Explicit solutions for linear viscoelastic rheologies can be computed using the correspondence principle. In order to consider the Maxwell rheology, we must employ the elastic parameters in the Laplace domain (e.g. Fung 1965):

$$\widetilde{K}(s) = K, \widetilde{\lambda}(s) = \frac{s\lambda + K\frac{\mu}{\eta}}{s + \frac{\mu}{\eta}}, \widetilde{\mu}(s) = \frac{\mu s}{s + \frac{\mu}{\eta}}, \widetilde{\nu}(s) = \frac{\widetilde{\lambda}(s)}{2\left[\widetilde{\lambda}(s) + \widetilde{\mu}(s)\right]} \tag{14}$$

where s is the Laplace variable and η the viscosity. Here and in the following, a superposed tilde denotes a quantity in the Laplace transform domain (a function of s, generally). The constitutive law for a viscoelastic material in the Laplace domain is formally equivalent to the one of an elastic material, accordingly:

$$\widetilde{\sigma}_{ij}(\mathbf{x}) = \begin{cases} \widetilde{\sigma}^s_{ij}(\mathbf{x}) + \widetilde{\sigma}^{ns}_{ij}(\mathbf{x}) - 3\widetilde{K}e_0\delta_{ij}, \; \mathbf{x} \in V_S \\ \widetilde{\sigma}^s_{ij}(\mathbf{x}) + \widetilde{\sigma}^{ns}_{ij}(\mathbf{x}), \; \mathbf{x} \notin V_S \end{cases}. \tag{15}$$

We consider the case in which the potency occurs suddenly inside the TPE inclusion, so that

$$\epsilon_0(t) = e_0\Theta(t), \tag{16}$$

where $\Theta(t)$ is the Heaviside step function and $\widetilde{\epsilon}_0 = e_0/s$.

3.1 TPVE solutions of the singular components

According to the correspondence principle, the singular components of displacement can be expressed in the Laplace domain substituting the constant A (9) with:

$$\widetilde{A}(s) = \frac{e_0}{s} \frac{3\widetilde{\lambda} + 2\widetilde{\mu}}{\widetilde{\lambda} + 2\widetilde{\mu}} \frac{d}{2a} \tag{17}$$

The inverse Laplace transform of (17) can be then computed as:

$$A(t) = \frac{3de_0}{2a} \left[1 - \frac{4\mu}{3\lambda + 6\mu} \exp\left(-\frac{2\mu + 3\lambda}{3\lambda + 6\mu} \frac{t}{\tau} \right) \right] \tag{18}$$

where $\tau = \eta/\mu$ is the Maxwell relaxation time.

Substituting the constant A in eq. (9) with the function $A(t)$ given by eq. (18) into eq. (8) we can obtain the viscoelastic solutions for the singular components of displacement:

$$u_r^s(\mathbf{r}, t) = \begin{cases} A(t)aS_1(\mathbf{r}) \text{ if } r < a \\ A(t)aS_2(\mathbf{r}) \text{ if } r > a \end{cases}, \quad u_\theta^s(\mathbf{r}, t) = \begin{cases} A(t)aS_3(\mathbf{r}) \text{ if } r < a \\ A(t)aS_4(\mathbf{r}) \text{ if } r > a \end{cases} \tag{19a}$$

The singular component of the viscoelastic strain tensor, $e^s(r, \theta, \varphi, t)$, can be also computed replacing in eq. (10) the expression of A (9) with the one of $A(t)$ (18):

$$e_{rr}^s(\mathbf{r}, t) = \begin{cases} A(t)S_5(\mathbf{r}) \text{ if } r < a \\ A(t)S_6(\mathbf{r}) \text{ if } r > a \end{cases}, \quad e_{\theta\theta}^s(\mathbf{r}, t) = \begin{cases} A(t)S_7(\mathbf{r}) \text{ if } r < a \\ A(t)S_8(\mathbf{r}) \text{ if } r > a \end{cases}, \tag{20a}$$

$$e_{\varphi\varphi}^s(\mathbf{r}, t) = \begin{cases} A(t)S_9(\mathbf{r}) \text{ if } r < a \\ A(t)S_{10}(\mathbf{r}) \text{ if } r > a \end{cases}, \quad e_{r\theta}^s(\mathbf{r}, t) = \begin{cases} A(t)S_{11}(\mathbf{r}) \text{ if } r < a \\ A(t)S_{12}(\mathbf{r}) \text{ if } r > a \end{cases}. \tag{20b}$$

According to eq (15), the computation of the singular viscoelastic stress components can be performed by computing the Laplace transform of the terms

$$\widetilde{L}_1(s) = \widetilde{\mu}\widetilde{A} \tag{21a}$$

$$\widetilde{L}_2(s) = \widetilde{\lambda}\widetilde{A} \tag{21b}$$

which give:

$$L_1(t) = \frac{\mu(3\lambda + 2\mu)de_0}{2a(\lambda + 2\mu)} \left[\exp\left(-\frac{2\mu + 3\lambda}{3\lambda + 6\mu} \frac{t}{\tau} \right) \right] \tag{22a}$$

$$L_2(t) = \frac{(3\lambda + 2\mu)de_0}{2a} \left[1 - \frac{2\mu}{\lambda + 2\mu} \exp\left(-\frac{2\mu + 3\lambda}{3\lambda + 6\mu} \frac{t}{\tau} \right) \right]. \tag{22b}$$

Accordingly, introducing for convenience $S_{r < a} = S_5 + S_7 + S_9$ and $S_{r > a} = S_6 + S_8 + S_{10}$:

$$\sigma_{rr}^s(\mathbf{r}, t) = \begin{cases} 2L_1(t)S_5(\mathbf{r}) + L_2(t)S_{r<a} \text{ if } r < a \\ 2L_1(t)S_6(\mathbf{r}) + L_2(t)S_{r>a} \text{ if } r > a \end{cases}, \quad \sigma_{\theta\theta}^s(\mathbf{r}, t) = \begin{cases} 2L_1(t)S_7(\mathbf{r}) + L_2(t)S_{r<a} \text{ if } r < a \\ 2L_1(t)S_8(\mathbf{r}) + L_2(t)S_{r>a} \text{ if } r > a \end{cases}, \tag{23a}$$

$$\sigma_{\varphi\varphi}^s(\mathbf{r}, t) = \begin{cases} 2L_1(t)S_9(\mathbf{r}) + L_2(t)S_{r<a} \text{ if } r < a \\ 2L_1(t)S_{10}(\mathbf{r}) + L_2(t)S_{r>a} \text{ if } r > a \end{cases}, \quad \sigma_{r\theta}^s(\mathbf{r}, t) = \begin{cases} 2L_1(t)S_{11}(\mathbf{r}) \text{ if } r < a \\ 2L_1(t)S_{12}(\mathbf{r}) \text{ if } r > a \end{cases}. \tag{23b}$$

3.1.1 From spherical to cartesian coordinates

Given the two rotation matrices, $\mathbf{Q}$ and $\mathbf{R}$

$$\mathbf{Q} = \begin{bmatrix} \sin\theta \cos\varphi & \cos\theta \cos\varphi & -\sin\varphi \\ \sin\theta \sin\varphi & \cos\theta \sin\varphi & \cos\varphi \\ \cos\theta & -\sin\theta & 0 \end{bmatrix} \tag{24}$$

$$\mathbf{R} = \begin{bmatrix} 1 & 0 & 0 \\ 0 & 1 & 0 \\ 0 & 0 & -1 \end{bmatrix} \tag{25}$$

at a given time, t, the displacement in the Cartesian reference system with the z axis pointing downwards, in which non-singular solutions are expressed, can be then computed as

$$\mathbf{u}^s(x, y, z, t) = \mathbf{RQu}^s(r, \theta, \varphi, t) \tag{26}$$

and the strain and the stress tensor, respectively as

$$\mathbf{e}^s(x, y, z, t) = \mathbf{RQe}^s(r, \theta, \varphi, t)\mathbf{Q}^T\mathbf{R}^T \tag{27}$$

$$\sigma^s(x, y, z, t) = \mathbf{R}\mathbf{Q}\sigma^s(r, \theta, \varphi, t)\mathbf{Q}^{\mathbf{T}}\mathbf{R}^{\mathbf{T}} \tag{28}$$

by considering that $r = \sqrt{x^2 + y^2 + (z - c)^2}$, $\sin\theta = \sqrt{x^2 + y^2}/r$, $\cos\theta = (z - c)/r$, $\sin\varphi = y/\sqrt{x^2 + y^2}$ and $\cos\varphi = x/\sqrt{x^2 + y^2}$.

3.2 TPVE solutions of the non-singular components

For the non-singular components of displacement, we must express both C and D coefficients in the Laplace domain as:

$$\widetilde{C}(s) = \frac{e_0}{s}\frac{3K(1-2\widetilde{\nu})}{8\pi\widetilde{\mu}(1-\widetilde{\nu})}(3 - 4\widetilde{\nu}) \tag{29a}$$

$$\widetilde{D}(s) = \frac{e_0}{s}\frac{3K(1-2\widetilde{\nu})}{8\pi\widetilde{\mu}(1-\widetilde{\nu})} \tag{29b}$$

and their inverse Laplace transforms are

$$C(t) = \frac{3e_0}{4\pi}\left[1 - \frac{2\mu}{(3\lambda+3\mu)}\exp\left(-\frac{2\mu+3\lambda}{3\lambda+3\mu}\frac{t}{\tau}\right) + \frac{4\mu}{3\lambda+6\mu}\exp\left(-\frac{2\mu+3\lambda}{3\lambda+6\mu}\frac{t}{\tau}\right)\right] \tag{30a}$$

$$D(t) = \frac{3e_0}{4\pi}\left[1 - \frac{4\mu}{(3\lambda+6\mu)}\exp\left(-\frac{2\mu+3\lambda}{3\lambda+6\mu}\frac{t}{\tau}\right)\right]. \tag{30b}$$

The viscoelastic solutions for the non-singular components can be computed as:

$$u_1^{ns}(\mathbf{x}, t) = C(t)I_a^{(1)}(\mathbf{x}) + D(t)I_b^{(1)}(\mathbf{x}) \tag{31a}$$

$$u_2^{ns}(\mathbf{x}, t) = C(t)I_a^{(2)}(\mathbf{x}) + D(t)I_b^{(2)}(\mathbf{x}) \tag{31b}$$

$$u_3^{ns}(\mathbf{x}, t) = -C(t)I_a^{(3)}(\mathbf{x}) - D(t)I_b^{(3)}(\mathbf{x}) \tag{31c}$$

The viscoelastic strain tensor can be computed replacing in eqs (13) by the expressions of C (12b) and D (12c) with $C(t)$ (30a) and $D(t)$ (30b), respectively:

$$e_{11}^{ns}(\mathbf{x}, t) = C(t)\frac{\partial I_a^{(1)}}{\partial x_1} + D(t)\frac{\partial I_b^{(1)}}{\partial x_1} \tag{32a}$$

$$e_{22}^{ns}(\mathbf{x}, t) = C(t)\frac{\partial I_a^{(2)}}{\partial x_2} + D(t)\frac{\partial I_b^{(2)}}{\partial x_2} \tag{32b}$$

$$e_{33}^{ns}(\mathbf{x}, t) = -C(t)\frac{\partial I_a^{(3)}}{\partial x_3} - D(t)\frac{\partial I_b^{(3)}}{\partial x_3} \tag{32c}$$

$$e_{13}^{ns}(\mathbf{x}, t) = \frac{C(t)}{2}\left(\frac{\partial I_a^{(1)}}{\partial x_3} + \frac{\partial I_a^{(3)}}{\partial x_1}\right) + \frac{D(t)}{2}\left(\frac{\partial I_b^{(1)}}{\partial x_3} + \frac{\partial I_b^{(3)}}{\partial x_1}\right) \tag{32d}$$

The non-singular viscoelastic stress components can be computed considering the viscoelastic relation (15) and (5), and computing the Laplace transform of the following terms

$$\widetilde{M}_1(s) = \widetilde{\mu}\widetilde{C} \tag{33a}$$

$$\widetilde{M}_2(s) = \widetilde{\lambda}\widetilde{C} \tag{33b}$$

$$\widetilde{M}_3(s) = \widetilde{\mu}\widetilde{D} \tag{33c}$$

$$\widetilde{M}_4(s) = \widetilde{\lambda}\widetilde{D} \tag{33d}$$

which give in the time domain:

$$M_1(t) = \frac{\mu(2\mu+3\lambda)e_0}{2\pi}\left[\frac{1}{\lambda+\mu}\exp\left(-\frac{2\mu+3\lambda}{3\lambda+3\mu}\frac{t}{\tau}\right) - \frac{1}{2(\lambda+2\mu)}\exp\left(-\frac{2\mu+3\lambda}{3\lambda+6\mu}\frac{t}{\tau}\right)\right] \tag{34a}$$

$$M_2(t) = \frac{(2\mu+3\lambda)e_0}{4\pi}\left[1 - \frac{2\mu}{\lambda+\mu}\exp\left(-\frac{2\mu+3\lambda}{3\lambda+3\mu}\frac{t}{\tau}\right) + \frac{2\mu}{\lambda+2\mu}\exp\left(-\frac{2\mu+3\lambda}{3\lambda+6\mu}\frac{t}{\tau}\right)\right] \tag{34b}$$

$$M_3(t) = \frac{\mu(2\mu+3\lambda)e_0}{4\pi(\lambda+2\mu)}\left[\exp\left(-\frac{2\mu+3\lambda}{3\lambda+6\mu}\frac{t}{\tau}\right)\right] \tag{34c}$$

$$M_4(t) = \frac{(2\mu+3\lambda)e_0}{4\pi}\left[1 - \frac{2\mu}{\lambda+2\mu}\exp\left(-\frac{2\mu+3\lambda}{3\lambda+6\mu}\frac{t}{\tau}\right)\right]. \tag{34d}$$

Accordingly,

$$\sigma_{11}^{ns}(\mathbf{x}, t) = 2M_1(t)\frac{\partial I_a^{(1)}}{\partial x_1} + 2M_3(t)\frac{\partial I_b^{(1)}}{\partial x_1} + M_2(t)\left(\frac{\partial I_a^{(1)}}{\partial x_1} + \frac{\partial I_a^{(2)}}{\partial x_2} - \frac{\partial I_a^{(3)}}{\partial x_3}\right) + M_4(t)\left(\frac{\partial I_b^{(1)}}{\partial x_1} + \frac{\partial I_b^{(2)}}{\partial x_2} - \frac{\partial I_b^{(3)}}{\partial x_3}\right) \tag{35a}$$

$$\sigma_{22}^{ns}(\mathbf{x}, t) = 2M_1(t)\frac{\partial I_a^{(2)}}{\partial x_2} + 2M_3(t)\frac{\partial I_b^{(2)}}{\partial x_2} + M_2(t)\left(\frac{\partial I_a^{(1)}}{\partial x_1} + \frac{\partial I_a^{(2)}}{\partial x_2} - \frac{\partial I_a^{(3)}}{\partial x_3}\right) + M_4(t)\left(\frac{\partial I_b^{(1)}}{\partial x_1} + \frac{\partial I_b^{(2)}}{\partial x_2} - \frac{\partial I_b^{(3)}}{\partial x_3}\right) \tag{35b}$$

$$\sigma_{33}^{ns}(\mathbf{x}, t) = -2M_1(t)\frac{\partial I_a^{(3)}}{\partial x_3} - 2M_3(t)\frac{\partial I_b^{(3)}}{\partial x_3} + M_2(t)\left(\frac{\partial I_a^{(1)}}{\partial x_1} + \frac{\partial I_a^{(2)}}{\partial x_2} - \frac{\partial I_a^{(3)}}{\partial x_3}\right) + M_4(t)\left(\frac{\partial I_b^{(1)}}{\partial x_1} + \frac{\partial I_b^{(2)}}{\partial x_2} - \frac{\partial I_b^{(3)}}{\partial x_3}\right) \tag{35c}$$

$$\sigma_{13}^{ns}(\mathbf{x}, t) = M_1(t)\left(\frac{\partial I_a^{(1)}}{\partial x_3} + \frac{\partial I_a^{(3)}}{\partial x_1}\right) + M_3(t)\left(\frac{\partial I_b^{(1)}}{\partial x_3} + \frac{\partial I_b^{(3)}}{\partial x_1}\right). \tag{35d}$$

3.3 Complete solutions

The the total viscoelastic displacement can be then computed as:

$$u_i(\mathbf{x}, t) = u_i{}^s(\mathbf{x}, t) + u_i{}^{ns}(\mathbf{x}, t) \tag{36}$$

As for the displacement, the total strain is obtained by summing the singular and the non-singular strain tensor:

$$e_{ij}(\mathbf{x}, t) = e_{ij}{}^s(\mathbf{x}, t) + e_{ij}{}^{ns}(\mathbf{x}, t). \tag{37}$$

For the stress tensor, we must consider that an additional term appears inside the TPE inclusion, so that:

$$\sigma_{ij}(\mathbf{x}, t) = \begin{cases} \sigma_{ij}^s(\mathbf{x}, t) + \sigma_{ij}^{ns}(\mathbf{x}, t) - 3Ke_0\delta_{ij}\Theta(t) \,, & \mathbf{x} \in V_S \\ \sigma_{ij}^s(\mathbf{x}, t) + \sigma_{ij}^{ns}(\mathbf{x}, t) & , \ \mathbf{x} \notin V_S \end{cases}. \tag{38}$$

Notice that the term $3Ke_0\delta_{ij}$ is the same appearing in the elastic solution. The complete viscoelastic displacement, stress and strain components are shown in Fig. 3 for a test case TPE inclusion with radius $a = 2500$ m, width $d = 500$ m located at a depth $c = 2000$ m (e.g. Nespoli *et al.* 2021). Results are shown at the surface ($z = 0$, Figs 3a, c and e) and on the median plane of the inclusion ($z = c$, Figs 3b, d and f) for three different instants ($t/\tau = 0$, 0.5 and 2). In Fig. 4 the verticals sections of maximum shear stress and displacement are plotted for $t/\tau = 0$, 2 and 4, showing a drastic reduction of the shear stress in the whole half-space. In Fig. 4d, the vertical component of the surface displacement, $u_z(x, y = z = 0, t)$, is plotted as function of the normalized time t/τ, together with the maximum shear stress computed in the centre ($x = 0$, $y = 0$, $z = c$) of the TPE inclusion. According to the used Maxwell's viscoelastic rheology, the uplift increases over time progressively reducing its growth rate. The shear stress, instead, has an opposite behaviour as it reduces over time. This result is different with respect to the response expected in an elastic scenario, where an increase of uplift would be accompanied by an increase of shear stress (hence seismicity), and vice versa (e.g. Belardinelli *et al.* 2011).

4 DISCUSSION

The surface displacement gives strong constraints on processes occurring at depth. Moreover, the rapid advancement of technology has allowed us to measure its temporal evolution with an accuracy of a few millimetres (e.g. with Global Navigation Satellite System) and to capture detailed images of its spatial pattern (e.g. with the Interferometric Synthetic Aperture Radar). Another important geophysical evidence is the presence of seismicity. According to the theory of faulting, the occurrence of earthquakes is strongly coupled with variations in the stress field. The stress is linked to the strain, which is related in turn to the soil uplift, through an appropriate constitutive relationship (e.g. elastic, poro-elastic and viscoelastic). A scientific challenge of a large part of both past and recent geophysical literature aims to disclose which source of deformation can explain such evidences (see Bonafede *et al.* 2022 and ref. therein). Understanding the actual deformation source does not have the sole purpose of filling a scientific curiosity but has also crucial implications for the correct estimation of the geohazard of the study area. Clearly, the greater the detail with which the deformation source model is known, the greater the chances of being able to discriminate between the different types of sources. Moreover, it is also very important to exploit large and multitechnique data sets mapping the active deformation, since sophisticated models can be only constrained with reasonable reliability by high quality data.

This work extends the applicability of the disc shaped TPE inclusions to viscoelastic media. Such an improvement is important to model the observed transient effects on displacement and seismicity, which could not be simply explained with a purely elastic model. Drawing inspiration from the unrest phase occurred between 1982 and 1984 at Campi Flegrei, the viscoelastic rheology is here considered as a possible and effective mechanism to explain the time-lag, which may occur between the decrease of the seismicity rate and the end of the uplift phase, as it is was observed at Campi Flegrei (Fig. 1). In fact, according to the TPVE model, after an elastic phase of uplift, the viscoelastic response leads to a further increase of the uplift phase over time, which is accompanied by a progressive and significant reduction of the maximum shear stress (and seismicity) inside the inclusion (Fig. 4). Even if the maximum shear stress is greater inside the inclusion, its reduction over time is expected in the whole domain, supporting the evidence that the seismicity decreases over time both inside and outside the inclusion (Fig. 4). Assuming the same value of viscosity, $\eta = 10^{16}$ Pas, employed by Bonafede & Ferrari (2009) for the same study area and a rigidity of $\mu = 6$ GPa (e.g. Nespoli *et al.* 2021), the time-series of the uplift almost reaches its asymptote at $\tau = \eta/\mu = 4$, which corresponds to a period of about 2.5 months, compatible with what observed at the end of the '82–'84 unrest phase (Figs 4 b and c). In the same time interval, the uplift increases by about 15 cm, while the shear stress inside the inclusion drops by 87 per cent. While crustal viscosities in non-volcanic regions usually have an order of magnitude of $\eta = 10^{19}$–10^{21} Pas (e.g. Newman *et al.* 2001; Jellinek & DePaolo 2003); in volcanic zones, the viscosities are usually lower, reaching values up to $\eta = 10^{18}$–10^{19} Pas (e.g. Head *et al.* 2019). Even lower viscosities, down to $\eta \approx 10^{13}$
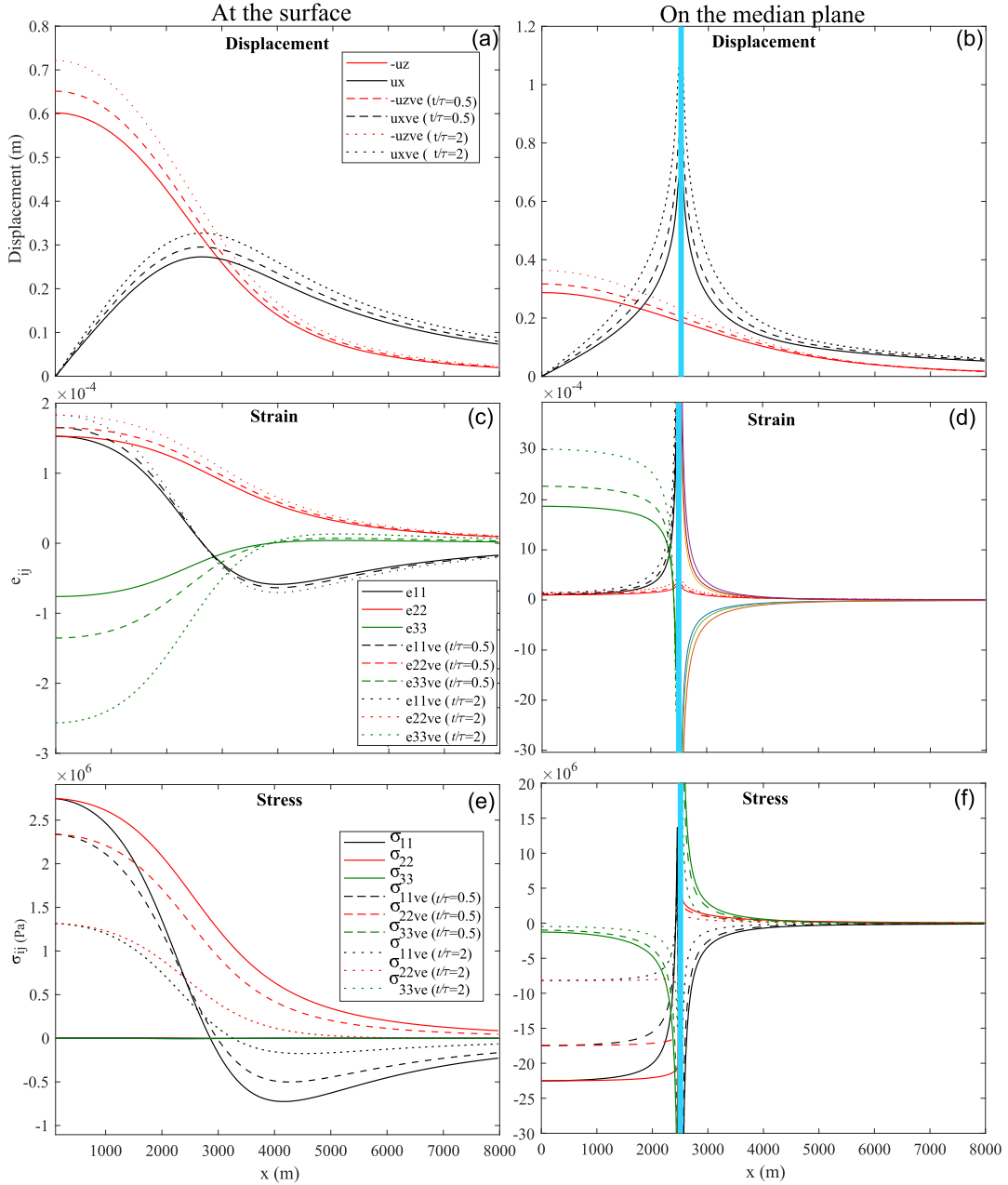
Figure 3. Viscoelastic displacements (a and b), strain (c and d) and stress (e and f) components generated by a disc-shaped TPE inclusion located at depth c = 2000 m, with radius a = 2500 m, width d = 500 m, Δp = 10 MPa and ΔT = 100 K. Curves in left-hand panels (a, c and e) are computed at the surface z = 0, while the ones in the right-hand panels are computed in the median plane of the inclusion (z = 2000 m). Quantities are shown for t/τ =0 (solid lines), 0.5 and 2. The light blue lines indicate the location of the lateral boundary of the inclusion. For the computation we use μ = 6 GPa and ν = 0.2 (K = 8 GPa).

Pas, can characterize the magma reservoir host rocks (e.g. Hickey *et al.* 2015). A viscosity of $\eta \approx 10^{16}$ Pas is suitable to represent magmatic "mush" zones (Hickey *et al.* 2015) and was employed by Dragoni & Magnanensi (1989) and Newman *et al.* (2001) to model viscoelastic shells surrounding magma chambers. Generally, low viscosities can be suitable to represent the ductile rocks surrounding a magmatic system (Jellinek & DePaolo 2003; Head *et al.* 2021), such as those embedding the TPVE inclusion considered in this work.

It would be interesting to see if at the end of the current unrest phase the viscoelasticity will play a role comparable to the one of the '82–'84 unrest phase. Instead, it is much more unlikely that the current unrest phase is completely due to transient viscoelastic effects. In fact, differently from what expected during the viscoelastic relaxation (Fig. 4), since 2005 both uplift and seismicity are increasing over time with an accelerating trend (e.g. Tramelli *et al.* 2021). Accordingly, the present state of the Campi Flegrei caldera seems to be related to the TPE effects induced by the hydrothermal circulation, although even a contribution to the deformation induced by magmatic sources cannot be excluded *a priori*. To better understand the actual phase of unrest, it would be interesting to study if and how both the uplift rate and the current seismicity can be explained in terms of increasing pore-pressure and temperature of the exsolved magmatic fluids inside the TPE inclusion.
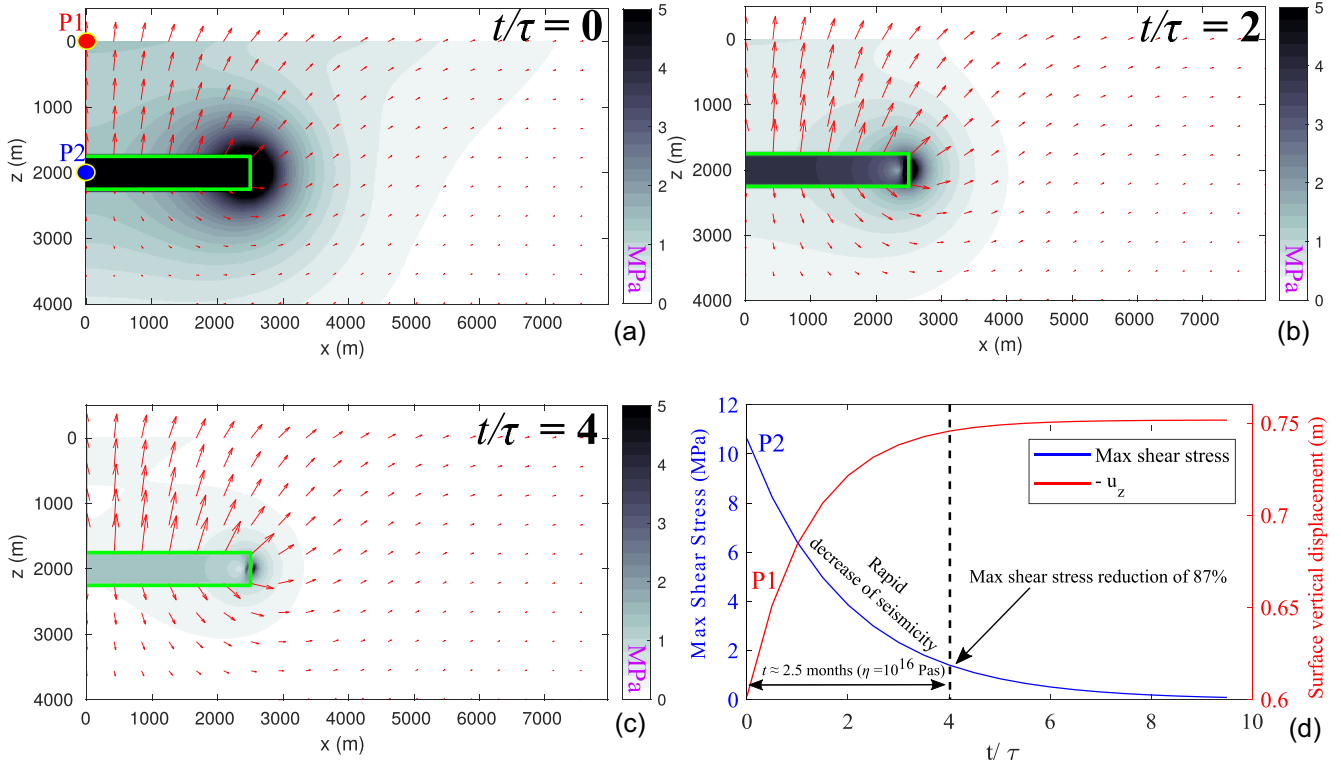
Figure 4. Vertical sections of maximum shear stress (colour) and displacement (m) exaggerated by a factor of 500 (red arrows) computed for $t/\tau = 0$ (a), 2 (b) and 4(c). The green line indicates the boundaries of the considered TPE inclusion. Panel (d) shows the time-series of displacement and maximum shear stress computed respectively in point P1($x = 0$ and $z = 0$) and in point P2($x = 0$ and $z = 2000$ m), respectively. The locations of the two points is also shown in panel (a). For the computation, we use $\mu = 6$ GPa and $\nu = 0.2$ ($K = 8$ GPa).

Although we are aware that the TPVE solutions proposed in this work are based on several simplifications, they indicate that the inclusion of the viscoelastic behaviour can be important for a complete interpretation of the data. Though we have taken as example the Campi Flegrei region, which is an area with a very extensive literature, we believe that our results can find application in other geothermal areas in which viscoelastic effects can occur as well (van Thienen-Visser & Fokker 2017).

The analytical formulas obtained in this work allow us to model the effects of an inclusion embedded in a homogeneous viscoelastic region. This poses a limit to represent more complex configurations in which the viscoelastic behaviour could be restricted within a particular layer of rock or to a volume of generic shape (e.g. Dragoni & Magnanensi 1989; Orlic & Wassing 2013; Marketos *et al.* 2015) or to the TPE inclusion volume only. In any case, it is undeniable that every numerical model with a greater complexity should be preliminarily set up and checked by using the analytical solutions obtained for a homogeneous medium. The solutions presented in this work consist of a first step for the representation of TPVE inclusions. Further improvements could be obtained by considering more complex temporal variations of the inclusion potency e_0 (eq. 2) with respect to the step-like variation considered in (16). The correspondence principle should also be easily applied for the case of a potency that linearly increase over time, similarly to what was done by Bonafede & Ferrari (2009) for the case of a Mogi sphere embedded in a viscoelastic space, with linearly increasing fluid pressure, or more general rheological relationships such as the SLS or the transient Burger's rheology. A further interesting improvement could consist including the effects of the fluid propagation inside the inclusion, following the approach proposed by Nespoli *et al.* (2021). This could lead to more complex transient effects on the deformation field produced by the inclusion.

5 CONCLUSIONS

The study of the buried deformation sources is very important for the creation of a realistic conceptual model of a study area and for the correct estimation of its geohazard. In this work, we integrate the viscoelastic behaviour with the mechanical solutions of a disc-shaped TPE inclusion. The present TPVE analytical solutions were obtained by using the correspondence principle and assuming that the medium is a homogeneous Maxwell half space. Such a generalization can be useful to represent transient effects of both deformation and stress fields that can occur in volcanic and geothermal areas, which would be difficult to explain otherwise. The most intriguing result indicates that a TPVE inclusion can represent a decrease in seismicity rate accompanied by an increase in surface uplift. This behaviour is in contrast with what is expected according to the elastic response, in which the seismicity increases during the uplift and decreases during the subsidence.

ACKNOWLEDGMENTS

Author contributions

Massimo Nespoli (conceptualization, formal analysis, methodology, software, visualization and writing original draft), Maria Elina Belardinelli (conceptualization, methodology, validation, writing-review and editing) and Maurizio Bonafede (conceptualization, methodology, validation, writing-review and editing).

DATA AVAILABILITY

The data shown in Figs 1 a–c are available upon request from the authors of Belardinelli *et al.* (2011). The long time-series shown in Fig. 1 d are available upon request from the authors of De Martino *et al.* (2021). Two MATLAB scripts, including the equations reported in this work, are available through the GitHub repository (https://github.com/Massimones/TPVE_solutions.git), and they are also accessible via Zenodo (https://zenodo.org/badge/latestdoi/636593573, doi:10.5281/zenodo.7898877).

REFERENCES

Aki, K. & Richards, P. G., 2002. *Quantitative seismology*. University Science Books. 2nd edition, volume 1.

Barberi, F., Corrado, G., Innocenti, F. & Luongo, G., 1984. Phlegraean fields 1982–1984: Brief chronicle of a volcano emergency in a densely populated area, *Bull. Volcanologique,* **47**(2), 175–185 . doi:10.1007/BF01961547.

Barbot, S., 2018. Deformation of a Half–Space from Anelastic Strain Confined in a Tetrahedral Volume, *Bull. seism. Soc. Am.,* **108**(5A), 2687–2712 . doi:10.1785/0120180058.

Belardinelli, M., Bizzarri, A., Berrino, G. & Ricciardi, G., 2011. A model for seismicity rates observed during the 1982-1984 unrest at Campi Flegrei caldera (italy), *Earth planet. Sci. Lett.,* **302**(3), 287–298 . doi:10.1016/j.epsl.2010.12.015.

Belardinelli, M., Bonafede, M. & Nespoli, M., 2019. Stress heterogeneities and failure mechanisms induced by temperature and pore-pressure increase in volcanic regions, *Earth planet. Sci. Lett.,* **525**, 115765.

Belardinelli, M. E., Nespoli, M. & Bonafede, M., 2022. Stress changes caused by exsolution of magmatic fluids within an axi-symmetric inclusion, *Geophys. J. Int.,* **230** (2), 870–892.

Bonafede, M. & Ferrari, C., 2009. Analytical models of deformation and residual gravity changes due to a mogi source in a viscoelastic medium, *Tectonophysics,* **471**(1–2), 4–13.

Bonafede, M., Amoruso, A., Crescentini, L., Gottsmann, J. H., Todesco, M. & Trasatti, E., 2022. Source Modelling from Ground Deformation and Gravity Changes at the Campi Flegrei Caldera, Italy, pp 283–309, In: *Campi Flegrei. Active Volcanoes of the World,* (eds) Orsi, G. D'Antonio, M. & Civetta, L. Springer Berlin Heidelberg, Berlin, Heidelberg. https://doi.org/10.1007/978-3-642-37060-1_11.

Calò, M. & Tramelli, A., 2018. Anatomy of the Campi Flegrei caldera using enhanced seismic tomography models, *Scientific Reports,* **8**(16254), doi:10.1038/s41598-018-34456-x.

Carlino, S., Somma, R., Troise, C. & Natale, G. D., 2012. The geothermal exploration of campanian volcanoes: historical review and future development, *Renewable Sustainable Energy Rev.,* **16**(1), 1004–1030 . doi:10.1016/j.rser.2011.09.023.

Chiodini, G. *et al.*, 2021. Hydrothermal pressure-temperature control on co2 emissions and seismicity at Campi Flegrei (italy), *J. Volc. Geotherm. Res.,* **414**, 107245. https://doi.org/10.1016/j.jvolgeores.2021.107245.

D'Auria, L., Massa, B., Cristiano, E., Gaudio, C. D., Giudicepietro, F., Ricciardi, G. & Ricco, C., 2014. Retrieving the stress field within the Campi Flegrei caldera (southern italy) through an integrated geodetical and seismological approach, *Pure Appl. Geophys.,* **172**(11), 3247–3263.

D'Auria, L. *et al.*, 2015. Magma injection beneath the urban area of Naples: a new mechanism for the 2012–2013 volcanic unrest at Campi Flegrei caldera, *Sci. Rep.,* **5**(1), 13100. https://doi.org/10.1038/srep13100.

De Martino, P., Dolce, M., Brandi, G., Scarpato, G. & Tammaro, U., 2021. The ground deformation history of the neapolitan volcanic area (Campi Flegrei caldera, somma–vesuvius volcano, and ischia island) from 20 years of continuous gps observations (2000–2019), *Remote Sensing,* **13**(14), 2725.https://doi.org/10.3390/rs13142725.

De Vivo, B., Rolandi, G., Gans, P., Calvert, A., Bohrson, W. A., Spera, F. & Belkin, H., 2001. New constraints on the pyroclastic eruptive history of the campanian volcanic plain (italy), *Mineral. Petrol.,* **73**(1), 47–65.

Del Gaudio, C., Aquino, I., Ricciardi, G. P., Ricco, C. & Scandone, R., 2010. Unrest episodes at Campi Flegrei: a reconstruction of vertical ground movements during 1905–2009, *J. Volc. Geotherm. Res.,* **195**(1), 48–56.

Di Vito, M. A., Isaia, R., Orsi, G., Southon, J. D., Vita, S. D., d'Antonio, M., Pappalardo, L. & Piochi, M., 1999. Volcanism and deformation since 12,000 years at the Campi Flegrei caldera (italy), *J. Volc. Geotherm. Res.,* **91**(2–4), 221–246.

Dragoni, M. & Magnanensi, C., 1989. Displacement and stress produced by a pressurized, spherical magma chamber, surrounded by a viscoelastic shell, *Phys. Earth planet. Inter.,* **56**(3), 316–328 . doi:10.1016/0031-9201(89)90166-0.

Eshelby, J. D., 1957. The determination of the elastic field of an ellipsoidal inclusion, and related problems, *Proc. R. Soc. Lond. A,* **241**(1226), 376–396.

Fung, Y., 1965. *Foundations of Solid Mechanics,* Prentice-Hall international series in dynamics, Kluwer Academic Publishers.

Geertsma, J., 1973. Land subsidence above compacting oil and gas reservoirs, *J. Petrol. Tech.,* **25**(06), 734–744 . doi:10.2118/3730-PA.

Goetze, C. & Evans, B., 1979. Stress and temperature in the bending lithosphere as constrained by experimental rock mechanics, *Geophys. J. Int.,* **59**(3), 463–478 . doi:10.1111/j.1365-246X.1979.tb02567.x.

Gratier, J.-P., Dysthe, D. K. & Renard, F., 2013. Chapter 2 - the role of pressure solution creep in the ductility of the earth's upper crust, in *Advances in Geophysics,* **54,** 47–179, ed. Dmowska, R., Elsevier. https://doi.org/10.1016/B978-0-12-380940-7.00002-0.

Guido, F. L., Antonellini, M. & Picotti, V., 2015. Modeling ground displacement above reservoirs undergoing fluid withdrawal/injection based on an ellipsoidal inhomogeneity model, *Int. J. Rock Mech. Mining Sci.,* **79**, 63–69 . doi:10.1016/j.ijrmms.2015.08.010.

Head, M., Hickey, J., Gottsmann, J. & Fournier, N., 2019. The influence of viscoelastic crustal rheologies on volcanic ground deformation: Insights from models of pressure and volume change, *J. geophys. Res.: Solid Earth,* **124**(8), 8127–8146 . doi:10.1029/2019JB017832.

Head, M., Hickey, J., Gottsmann, J. & Fournier, N., 2021. Exploring the impact of thermally controlled crustal viscosity on volcanic ground deformation, *J. geophys. Res.: Solid Earth,* **126**(8), e2020JB020724. https://doi.org/10.1029/2020JB020724.

Hickey, J., Gottsmann, J. & Mothes, P., 2015. Estimating volcanic deformation source parameters with a finite element inversion: The 2001–2002

unrest at cotopaxi volcano, ecuador, *J. geophys. Res.: Solid Earth,* **120**(3), 1473–1486 . doi:10.1002/2014JB011731.

Jellinek, A. M. & DePaolo, D. J., 2003. A model for the origin of large silicic magma chambers: precursors of caldera-forming eruptions, *Bull. Volc.,* **65**(5), 363–381 . doi:10.1007/s00445-003-0277-y.

Judenherc, S. & Zollo, A., 2004. The bay of Naples (southern italy): Constraints on the volcanic structures inferred from a dense seismic survey, *J. geophys. Res.: Solid Earth,* **109**(B10), doi:10.1029/2003JB002876.

Kazemi-Lari, M. A., Shaw, J. A., Wineman, A. S., Shimkunas, R., Jian, Z., Hegyi, B., Izu, L. & Chen-Izu, Y., 2021. A viscoelastic eshelby inclusion model and analysis of the cell-in-gel system, *Int. J. Eng. Sci.,* **165,** 103489. https://doi.org/10.1016/j.ijengsci.2021.103489.

Landry, W. & Barbot, S., 2019. Fast, accurate solutions for 3d strain volumes in a heterogeneous half space, *Comput. Geosci.,* **125,** 109–114 . doi:10.1016/j.cageo.2019.01.001.

Lima, A., PBodnar, R. J., De Vivo, B., Spera, F. & Belkin, H., 2021. Interpretation of recent unrest events (bradyseism) at Campi Flegrei, Napoli (italy): Comparison of models based on cyclical hydrothermal events versus shallow magmatic intrusive events, *Geofluids,* **2021**(2000255), 1–16 . doi:10.1155/2021/2000255.

Mantiloni, L., Nespoli, M., Belardinelli, M. E. & Bonafede, M., 2020. Deformation and stress in hydrothermal regions: The case of a disc-shaped inclusion in a half-space, *J. Volc. Geotherm. Res.,* **403,** 107011. https://doi.org/10.1016/j.jvolgeores.2020.107011.

Marketos, G., Govers, R. & Spiers, C., 2015. Ground motions induced by a producing hydrocarbon reservoir that is overlain by a viscoelastic rocksalt layer: a numerical model, *Geophys. J. Int.,* **203**(1), 228–242 . doi:10.1093/gji/ggv294.

Nespoli, M., Belardinelli, M. E. & Bonafede, M., 2021. Stress and deformation induced in layered media by cylindrical thermo-poro-elastic sources: An application to Campi Flegrei (italy), *J. Volc. Geotherm. Res.,* **415,** 107269. https://doi.org/10.1016/j.jvolgeores.2021.107269.

Nespoli, M., Belardinelli, M. E., Cal, M., Tramelli, A. & Bonafede, M., 2022. Deformation induced by distributions of single forces in a layered half-space: EFGRN/EFCMP, *Computers Geosci.,* **164,** 105136. https://doi.org/10.1016/j.cageo.2022.105136.

Newman, A., Dixon, T., Ofoegbu, G. & Dixon, J., 2001. Geodetic and seismic constraints on recent activity at long valley caldera, california: evidence for viscoelastic rheology, *J. Volc. Geotherm. Res.,* **105**(3), 183–206 . doi:10.1016/S0377-0273(00)00255-9.

Orlic, B. & Wassing, B. B. T., 2013. A study of stress change and fault slip in producing gas reservoirs overlain by elastic and viscoelastic caprocks, *Rock Mech. Rock Eng.,* **46**(3), 421–435 . doi:10.1007/s00603-012-0347-6.

Rudnicki, J., 1999. Alteration of regional stress by reservoirs and other inhomogeneities: stabilizing or destabilizing?, *Proceedings of the 9th International Congress on rock Mechanics 3,* ISRM-9CONGRESS-1999-303, pp 1629–1637.

Segall, P., 1989. Earthquakes triggered by fluid extraction, *Geology,* **17**(10), 942–946 . doi:10.1130/0091-7613(1989)017<0942:ETBFE>2.3.CO;2.

Segall, P., 1992. Induced stresses due to fluid extraction from axisymmetric reservoirs, *Pure appl. Geophys.,* **139**(3), 535–560 . doi:10.1007/BF00879950.

Segall, P. & Fitzgerald, S. D., 1998. A note on induced stress changes in hydrocarbon and geothermal reservoirs, *Tectonophysics,* **289**(1), 117–128 . doi:10.1016/S0040-1951(97)00311-9.

Todesco, M., 2021. Caldera's breathing: Poroelastic ground deformation at Campi Flegrei (italy), *Front. Earth Sci.,* **9,** 691 . doi:10.3389/feart.2021.702665.

Tramelli, A., Godano, C., Ricciolino, P., Giudicepietro, F., Caliro, S., Orazi, M., De Martino, P. & Chiodini, G., 2021. Statistics of seismicity to investigate the Campi Flegrei caldera unrest, *Sci. Rep.,* **11**(1), 7211 . doi:10.1038/s41598-021-86506-6.

Tramelli, A., Giudicepietro, F., Ricciolino, P. & Chiodini, G., 2022. The seismicity of Campi Flegrei in the contest of an evolving long term unrest, *Sci. Rep.,* **12**(1), 2900. https://doi.org/10.1038/s41598-022-06928-8.

Trasatti, E., Bonafede, M., Ferrari, C., Giunchi, C. & Berrino, G., 2011. On deformation sources in volcanic areas: modeling the Campi Flegrei (italy) 1982–84 unrest, *Earth planet. Sci. Lett.,* **306**(3–4), 175–185.

van Thienen-Visser, K. & Fokker, P. A., 2017. The future of subsidence modelling: compaction and subsidence due to gas depletion of the groningen gas field in the netherlands, *Netherlands J. Geosci.,* **96**(5), s105–s116 . doi:10.1017/njg.2017.10.

Wang, K., 2021. If Not Brittle: Ductile, Plastic, or Viscous?, *Seism. Res. Lett.,* **92**(2A), 1181–1184 . doi:10.1785/0220200242.

APPENDIX A: APPENDIX: COEFFICIENTS OF DISPLACEMENT AND STRAIN

A1 Singular components of displacement

Employing spherical coordinates $\mathbf{r} = (r, \theta, \varphi)$ and Legendre polynomials, P_{2m}:

$$S_1(\mathbf{r}) = -\sum_{m=0}^{\infty} c_{2m} P_{2m}(x) \left[\left(\frac{1}{2m+2} + \frac{1}{2m-1} \right) - \frac{2m}{2m-1} \left(\frac{r}{a} \right)^{2m-1} \right] \quad \text{if } r < a \tag{A1}$$

$$S_2(\mathbf{r}) = \sum_{m=0}^{\infty} c_{2m} P_{2m}(x) \frac{2m+1}{2m+2} \left(\frac{a}{r} \right)^{2m+2} \quad \text{if } r > a \tag{A2}$$

while the polar component of displacement is

$$S_3(\mathbf{r}) = -\sum_{m=1}^{\infty} c_{2m} \frac{\mathrm{d}P_{2m}(x)}{\mathrm{d}\theta} \left[\left(\frac{1}{2m+2} + \frac{1}{2m-1} \right) - \frac{1}{2m-1} \left(\frac{r}{a} \right)^{2m-1} \right] \quad \text{if } r < a \tag{A3}$$

$$S_4(\mathbf{r}) = -\sum_{m=1}^{\infty} c_{2m} \frac{\mathrm{d}P_{2m}(x)}{\mathrm{d}\theta} \left[\frac{1}{2m+2} \left(\frac{a}{r} \right)^{2m+2} \right] \quad \text{if } r > a \tag{A4}$$

and c_{2m} can be expressed as following:

$$c_\ell \equiv P_\ell(0) = \begin{cases} \frac{(-1)^m}{4^m} \frac{(2m)!}{(m!)^2} & \text{if } \ell = 2m \\ 0 & \text{if } \ell = 2m+1 \end{cases} \quad m = 0, 1, 2, \ldots \tag{A5}$$

A2 Singular components of strain

$$S_5(\mathbf{r}) = \sum_{m=1}^{\infty} 2m c_{2m} P_{2m}(x) \left[\frac{r}{a}\right]^{2m-2} \quad \text{if } r < a \tag{A6}$$

$$S_6(\mathbf{r}) = -\sum_{m=0}^{\infty} (2m+1) c_{2m} P_{2m}(x) \left[\frac{a}{r}\right]^{2m+3} \quad \text{if } r > a \tag{A7}$$

$$S_7(\mathbf{r}) = \left\{ 2\delta(x)\frac{a}{r} + \sum_{m=1}^{\infty} \frac{c_{2m}}{2m-1} \left(\frac{r}{a}\right)^{2m-2} \left[\frac{\mathrm{d}^2 P_{2m}}{\mathrm{d}\theta^2} + 2m P_{2m}\right] \right\} \quad \text{if } r < a \tag{A8}$$

$$S_8(\mathbf{r}) = \left\{ \frac{1}{2}\left(\frac{a}{r}\right)^3 + \sum_{m=1}^{\infty} \frac{c_{2m}}{2m+2} \left(\frac{a}{r}\right)^{2m+3} \left[(2m+1)P_{2m} - \frac{\mathrm{d}^2 P_{2m}}{\mathrm{d}\theta^2}\right] \right\} \quad \text{if } r > a \tag{A9}$$

$$S_9(\mathbf{r}) = \sum_{m=1}^{\infty} \frac{c_{2m}}{2m-1} \left(\frac{r}{a}\right)^{2m-2} \left[2m P_{2m} + \frac{\cos\theta}{\sin\theta}\frac{\mathrm{d}P_{2m}}{\mathrm{d}\theta}\right] \quad \text{if } r < a \tag{A10}$$

$$S_{10}(\mathbf{r}) = \sum_{m=0}^{\infty} \frac{c_{2m}}{2m+2} \left(\frac{a}{r}\right)^{2m+3} \left[(2m+1)P_{2m} - \frac{\cos\theta}{\sin\theta}\frac{\mathrm{d}P_{2m}}{\mathrm{d}\theta}\right] \quad \text{if } r > a \tag{A11}$$

$$S_{11}(\mathbf{r}) = \sum_{m=1}^{\infty} c_{2m} \frac{\mathrm{d}P_{2m}}{\mathrm{d}\theta} \left(\frac{r}{a}\right)^{2m-2} \quad \text{if } r < a \tag{A12}$$

$$S_{12}(\mathbf{r}) = \sum_{m=1}^{\infty} c_{2m} \frac{\mathrm{d}P_{2m}}{\mathrm{d}\theta} \left(\frac{a}{r}\right)^{2m+3} \quad \text{if } r > a \tag{A13}$$

A3 Non-singular components of displacement

$$I_a^{(1)}(\mathbf{x}) = \int_{-a}^{a} \mathrm{d}x_2' \left[\ln\left(\frac{R_2|_{c+\frac{\mathrm{d}}{2}}^{+} + x_3 + c + \frac{\mathrm{d}}{2}}{R_2|_{c-\frac{\mathrm{d}}{2}}^{+} + x_3 + c - \frac{\mathrm{d}}{2}}\right) - \ln\left(\frac{R_2|_{c+\frac{\mathrm{d}}{2}}^{-} + x_3 + c + \frac{\mathrm{d}}{2}}{R_2|_{c-\frac{\mathrm{d}}{2}}^{-} + x_3 + c - \frac{\mathrm{d}}{2}}\right) \right] \tag{A14}$$

$$I_b^{(1)}(\mathbf{x}) = 2x_3 \int_{-a}^{a} \mathrm{d}x_2' \left[\frac{1}{R_2|_{c+\frac{\mathrm{d}}{2}}^{+}} - \frac{1}{R_2|_{c+\frac{\mathrm{d}}{2}}^{-}} - \frac{1}{R_2|_{c-\frac{\mathrm{d}}{2}}^{+}} + \frac{1}{R_2|_{c-\frac{\mathrm{d}}{2}}^{-}} \right] \tag{A15}$$

$$I_a^{(2)}(\mathbf{x}) = \int_{-a}^{a} \mathrm{d}x_1' \int_{-f(x_1')}^{f(x_1')} (x_2 - x_2') \,\mathrm{d}x_2' \int_{c-\frac{\mathrm{d}}{2}}^{c+\frac{\mathrm{d}}{2}} \mathrm{d}x_3' \frac{1}{R_2^3} \tag{A16}$$

$$I_b^{(2)}(\mathbf{x}) = -\int_{-a}^{a} \mathrm{d}x_1' \int_{-f(x_1')}^{f(x_1')} (x_2 - x_2') \,\mathrm{d}x_2' \int_{c-\frac{\mathrm{d}}{2}}^{c+\frac{\mathrm{d}}{2}} \mathrm{d}x_3' \frac{6x_3(x_3 + x_3')}{R_2^5} \tag{A17}$$

$$I_a^{(3)}(\mathbf{x}) = -\int_{-a}^{a} \mathrm{d}x_2' \left[\ln\left(\frac{R_2^+|_{c+\frac{\mathrm{d}}{2}} - x_1 + f(x_2')}{R_2^-|_{c+\frac{\mathrm{d}}{2}} - x_1 - f(x_2')}\right) - \ln\left(\frac{R_2^+|_{c-\frac{\mathrm{d}}{2}} - x_1 + f(x_2')}{R_2^-|_{c-\frac{\mathrm{d}}{2}} - x_1 - f(x_2')}\right) \right] \tag{A18}$$

$$I_b^{(3)}(\mathbf{x}) = 2x_3 \left(x_3 + c + \frac{\mathrm{d}}{2}\right) \int_{-a}^{a} \mathrm{d}x_2' \frac{1}{(x_2 - x_2')^2 + (x_3 + c + \frac{\mathrm{d}}{2})^2} \left[\frac{x_1 - f(x_2')}{R_2^+|_{c+\frac{\mathrm{d}}{2}}} - \frac{x_1 + f(x_2')}{R_2^-|_{c+\frac{\mathrm{d}}{2}}}\right] -$$

$$-2x_3 \left(x_3 + c - \frac{\mathrm{d}}{2}\right) \int_{-a}^{a} \mathrm{d}x_2' \frac{1}{(x_2 - x_2')^2 + (x_3 + c - \frac{\mathrm{d}}{2})^2} \left[\frac{x_1 - f(x_2')}{R_2^+|_{c-\frac{\mathrm{d}}{2}}} - \frac{x_1 + f(x_2')}{R_2^-|_{c-\frac{\mathrm{d}}{2}}}\right] \tag{A19}$$

where

$$R_2 = \sqrt{(x_1 - x_1')^2 + (x_2 - x_2')^2 + (x_3 + x_3')^2}, \quad f(p) \doteq \sqrt{a^2 - p^2} \tag{A20}$$

and the functions $R_2^\pm$ are defined as the following:

$$R_2^+ (\mathbf{x}, x_2', x_3') = R_2 (\mathbf{x}, x_1' = +f(x_2'), x_2', x_3') \tag{A21a}$$

$$R_2^- (\mathbf{x}, x_2', x_3') = R_2 (\mathbf{x}, x_1' = -f(x_2'), x_2', x_3') \tag{A21b}$$

while the notation $R_2|_{(c\pm\frac{d}{2})}^\pm$ means $R_2^\pm$ evaluated at point $x_3' = c \pm \frac{d}{2}$, respectively, so:

$$R_2^+|_{c\pm\frac{d}{2}} (\mathbf{x}, x_2') = R_2^+ (\mathbf{x}, x_2', x_3' = c \pm \tfrac{d}{2}) \tag{A22a}$$

$$R_2^-|_{c\pm\frac{d}{2}} (\mathbf{x}, x_2') = R_2^- (\mathbf{x}, x_2', x_3' = c \pm \tfrac{d}{2}) \tag{A22b}$$

A4 Non-singular components of strain

$$\frac{\partial}{\partial x_1} I_a^{(1)} = -\int_{-a}^{a} dx_2' \frac{x_1 - f(x_2')}{(x_2 - x_2')^2 + (x_1 - f(x_2'))^2} \left(\frac{x_3 + c + \frac{d}{2}}{R_2^+|_{c+\frac{d}{2}}} - \frac{x_3 + c - \frac{d}{2}}{R_2^+|_{c-\frac{d}{2}}} \right) +$$

$$+ \int_{-a}^{a} dx_2' \frac{x_1 + f(x_2')}{(x_2 - x_2')^2 + (x_1 + f(x_2'))^2} \left(\frac{x_3 + c + \frac{d}{2}}{R_2^-|_{c+\frac{d}{2}}} - \frac{x_3 + c - \frac{d}{2}}{R_2^-|_{c-\frac{d}{2}}} \right) \tag{A23}$$

$$\frac{\partial}{\partial x_1} I_b^{(1)} = -2x_3 \int_{-a}^{a} dx_2' \left(\frac{x_1 - f(x_2')}{R_2^+|_{c+\frac{d}{2}}^3} - \frac{x_1 - f(x_2')}{R_2^+|_{c-\frac{d}{2}}^3} - \frac{x_1 + f(x_2')}{R_2^-|_{c+\frac{d}{2}}^3} + \frac{x_1 + f(x_2')}{R_2^-|_{c-\frac{d}{2}}^3} \right) \tag{A24}$$

$$\frac{\partial}{\partial x_2} I_a^{(2)} = 2 \int_{-a}^{a} dx_1' \frac{f(x_1')}{(x_1 - x_1')^2 + (x_2 - f(x_1')^2)} \left(\frac{x_3 + c + \frac{d}{2}}{R_2^+|_{c+\frac{d}{2}}} - \frac{x_3 + c - \frac{d}{2}}{R_2^+|_{c-\frac{d}{2}}} \right) + \tag{A25}$$

$$\frac{\partial}{\partial x_2} I_b^{(2)} = 4x_3 \int_{-a}^{a} dx_1' f(x_1') \left(\frac{1}{(R_2^+)^3|_{c+\frac{d}{2}}} - \frac{1}{(R_2^+)^3|_{c-\frac{d}{2}}} \right) \tag{A26}$$

$$\frac{\partial}{\partial x_3} I_a^{(3)} = -\int_{-a}^{a} dx_2' \left\{ -\left(x_3 + c + \frac{d}{2}\right) \left[-\frac{x_1 - f(x_2')}{[(x_2 - x_2')^2 + (x_3 + c + \frac{d}{2})^2]R_2^+|_{c+\frac{d}{2}}} \right. \right.$$

$$\left. + \frac{x_1 + f(x_2')}{[(x_2 - x_2')^2 + (x_3 + c + \frac{d}{2})^2]R_2^-|_{c+\frac{d}{2}}} \right] - \left(x_3 + c - \frac{d}{2}\right)$$

$$\left. \left[\frac{x_1 - f(x_2')}{[(x_2 - x_2')^2 + (x_3 + c - \frac{d}{2})^2]R_2^+|_{c-\frac{d}{2}}} - \frac{x_1 + f(x_2')}{[(x_2 - x_2')^2 + (x_3 + c - \frac{d}{2})^2]R_2^-|_{c-\frac{d}{2}}} \right] \right\} \tag{A27}$$

$$\frac{\partial}{\partial x_3} I_b^{(3)} = -2 \int_{-a}^{a} dx_2' \int_{-\sqrt{a^2 - (x_2')^2}}^{\sqrt{a^2 - (x_2')^2}} dx_1' \left\{ \frac{x_3 + c + \frac{d}{2}}{R_2^3|_{c+\frac{d}{2}}} - \frac{x_3 + c - \frac{d}{2}}{R_2^3|_{c-\frac{d}{2}}} + \frac{x_3}{R_2^3|_{c+\frac{d}{2}}} - \frac{x_3}{R_2^3|_{c-\frac{d}{2}}} + \right.$$

$$\left. - \frac{3x_3 (x_3 + c + \frac{d}{2})^2}{R_2^5|_{c+\frac{d}{2}}} + \frac{3x_3 (x_3 + c - \frac{d}{2})^2}{R_2^5|_{c-\frac{d}{2}}} \right\} \tag{A28}$$

$$\frac{\partial I_a^{(1)}}{\partial x_3} = \int_{-a}^{a} dx_2' \left(\frac{1}{R_2^+|_{c+\frac{d}{2}}} - \frac{1}{R_2^+|_{c-\frac{d}{2}}} - \frac{1}{R_2^-|_{c+\frac{d}{2}}} + \frac{1}{R_2^-|_{c-\frac{d}{2}}} \right) \tag{A29}$$

$$\frac{\partial I_b^{(1)}}{\partial x_3} = 2 \int\limits_{-a}^{a} \mathrm{d}x_2' \left[\frac{1}{R_2^+|_{c+\frac{d}{2}}} - \frac{1}{R_2^+|_{c-\frac{d}{2}}} - \frac{1}{R_2^-|_{c+\frac{d}{2}}} + \frac{1}{R_2^-|_{c-\frac{d}{2}}} - x_3 \left(\frac{x_3 + c + \frac{d}{2}}{\left(R_2^+|_{c+\frac{d}{2}} \right)^3} - \frac{x_3 + c - \frac{d}{2}}{\left(R_2^+|_{c-\frac{d}{2}} \right)^3} + \right. \right.$$

$$\left. \left. - \frac{x_3 + c + \frac{d}{2}}{\left(R_2^-|_{c+\frac{d}{2}} \right)^3} + \frac{x_3 + c - \frac{d}{2}}{\left(R_2^-|_{c-\frac{d}{2}} \right)^3} \right) \right] \tag{A30}$$

$$\frac{\partial I_a^{(3)}}{\partial x_1} = - \int\limits_{-a}^{a} \mathrm{d}x_2' \left\{ \left[\frac{1}{R_2^+|_{c+\frac{d}{2}}} - \frac{1}{R_2^-|_{c+\frac{d}{2}}} - \frac{1}{R_2^+|_{c-\frac{d}{2}}} + \frac{1}{R_2^-|_{c-\frac{d}{2}}} \right] \right\} \tag{A31}$$